crystals

MDPI

Article

ZnO-Assisted Synthesis of Rouaite ($Cu_2(OH)_3NO_3$) Long Hexagonal Multilayered Nanoplates Towards Catalytic Wet Peroxide Oxidation Application

Guang Yao Zhou [1], Jun Guo [2] and Ji Hong Wu [1,*]

[1] College of Chemistry, Chemical Engineering and Materials Science, Soochow University, 199 RenAi Road, Suzhou 215123, China; 20184209081@alu.suda.edu.cn
[2] Testing & Analysis Center, Soochow University, 199 RenAi Road, Suzhou 215123, China; guojun@suda.edu.cn
* Correspondence: wujh@suda.edu.cn

Abstract

Rouaite ($Cu_2(OH)_3NO_3$) long hexagonal multilayered nanoplates with high purity and high crystallinity were prepared from acidic reaction solution (pH = 4.4–4.8) with the assistance of ZnO. The ZnO-assisted strategy is remarkably different from the conventional synthetic protocol that was regularly carried out in alkaline solution (pH > 11). The rouaite multilayer nanoplates displayed exceptionally high catalytic activity in the catalytic wet peroxide oxidation (CWPO) of Congo red (CR). The catalytic efficiency for CR decolorization achieved an impressive 96.3% in 50 min under near-neutral (pH = 6.76) and ambient conditions (T = 20 °C, p = 1 atm), without increasing the temperature and/or decreasing the pH value to acidic region (pH = 2–3) as is commonly employed in CWPO process for improved degradation efficiency.

Keywords: catalytic wet peroxide oxidation; Congo red; multilayered nanoplates; rouaite

check for updates

Academic Editor: Leonid Kustov

Received: 11 July 2025
Revised: 30 July 2025
Accepted: 31 July 2025
Published: 2 August 2025

Citation: Zhou, G.Y.; Guo, J.; Wu, J.H. ZnO-Assisted Synthesis of Rouaite ($Cu_2(OH)_3NO_3$) Long Hexagonal Multilayered Nanoplates Towards Catalytic Wet Peroxide Oxidation Application. *Crystals* **2025**, *15*, 710. https://doi.org/10.3390/cryst15080710

Copyright: © 2025 by the authors. Licensee MDPI, Basel, Switzerland. This article is an open access article distributed under the terms and conditions of the Creative Commons Attribution (CC BY) license (https://creativecommons.org/licenses/by/4.0/).

1. Introduction

The rapid development of modern industry has led to the production and discharge of a huge amount of industrial wastewater containing various hazardous contaminants, which greatly threaten the ecological system and are harmful to human health [1]. In particular, the wastewater from the textile and printing industry contains a lot of organic dyes, such as azo dyes [2]. The dyes adsorb the light and greatly limit the light transparency of water [3]. They also consume water-dissolved oxygen and decrease the oxygen content of water [3]. In addition, azo dyes have been documented as a human carcinogen [4,5]. The hazard of azo dyes to human health includes asthmatic reactions, allergies, DNA damage, and hyperactivity [4,5]. Therefore, developing effective technology for removal of azo dyes is imperative for safe and healthy water resources.

Many technologies have been developed for azo dye removal, including adsorption [6], extraction [7], membrane separation [8], and ion exchange [9]. However, these technologies can only remove the azo dyes from the wastewater, but cannot destruct their structures. The biological treatment is not effective because the azo dyes are toxic to the microorganisms employed in the biological methods [10]. To this end, much attention has been paid to develop the technologies that can effectively destruct the structure and thus realize complete degradation of azo dyes. Advanced oxidation processes (AOP_S), known as a destructive chemical technology, have received increasing interests in the field of wastewater remediation, particularly for destructive degradation of organic contaminants [11–13]. Despite

the great promise of AOP technology, there are still challenges that should be overcome. Designing and synthesizing advanced catalysts with high intrinsic catalytic activity and abundant active sites is of great importance for the AOP catalytic performance. Intensive endeavor has been devoted to design and synthesize the advanced AOP catalysts [11]. Enriching the catalysts with abundant active sites by rationally designing their distinctive nanostructure is of vital significance for the catalytic performance [14–16]. Two-dimensional (2D) nanostructures, with a larger surface-to-volume ratio and unique mechanical stability, have attracted great interest [17,18].

In addition to the light employed in photocatalysis, the AOP technologies also widely employ various oxidants to boost the catalytic redox reactions, including oxygen (O_2) [19], ozone (O_3) [20], and hydrogen peroxide (H_2O_2) [21]. Among them, H_2O_2 is a promising oxidant as it has excellent catalytic performance, good water solubility, and environmental safety [22]. The AOP process employs H_2O_2 as the oxidant and is also known as catalytic wet peroxide oxidation (CWPO) [23–27]. Copper(II)-based hydroxide salts have been reported as a promising catalyst with high intrinsic CWPO catalytic activity [28,29]. Our group has reported the flowerlike nanoplate superstructures of brochantite ($Cu_4(OH)_6SO_4$) for CWPO treatment of Congo red (CR) [30]. The CR decolorization efficiency by the brochantite catalyst reached 97% in 2 h under near-neutral (pH = 6.4) and ambient conditions (T = 20 °C, p = 1 atm). In this work we extended the CWPO degradation of CR to another copper hydroxide salt, namely, rouaite ($Cu_2(OH)_3NO_3$). The rouaite catalyst exhibited improved catalytic performance compared to the brochantite catalyst. The catalytic efficiency of rouaite reached 96.3% in 50 min towards CR decolorization under near-neutral (pH = 6.76) and ambient conditions (T = 20 °C, p = 1 atm). The CR decolorization was accomplished without increasing the temperature and/or decreasing the pH value to the acidic region (pH = 2–3) as is commonly utilized in the CWPO process [31,32]. Note that the H_2O_2 dosage used in the rouaite-catalyzed CWPO reactions is only 50 μL, which is only 1/4 of the H_2O_2 dosage (0.2 mL) used in the brochantite-catalyzed CWPO reactions [30].

In the literature, $Cu_2(OH)_3NO_3$ is often prepared by precipitation in alkaline solution with pH > 11 [33,34]. The precipitation method is easy to handle and quite a large amount of $Cu_2(OH)_3NO_3$ product can be obtained from a single batch within a short time. However, the shortages of precipitation are also noteworthy. In most cases, the morphology of the $Cu_2(OH)_3NO_3$ product was poorly controlled [28,35]. The $Cu_2(OH)_3NO_3$ products prepared by precipitation often contain impurities, such as $Cu(OH)_2$ and CuO, if the pH value is not well controlled [28]. Systematic work on the synthesis of $Cu_2(OH)_3NO_3$ catalyst with well-defined 2D nanostructures towards CWPO application is rare in the literature. Herein we report a ZnO-assisted synthetic protocol for preparing the rouaite catalyst and apply it as the CWPO heterogeneous catalyst for CR degradation. The rouaite catalyst, with a well-defined long hexagonal multilayered nanoplate shape, high purity, and high crystallinity, was prepared from acidic reaction solution (pH = 4.4–4.8) with the assistance of ZnO. The ZnO-assisted synthetic protocol presents a remarkable distinction from previous reports, in which rouaite was routinely synthesized by the precipitation method from alkaline solution with pH > 11 [33,34]. The 2D nanoplate structural feature with a large surface-to-volume ratio and unique mechanical stability favorably boosted the high CWPO performance of rouaite.

2. Experimental Details

2.1. Chemicals and Materials

Copper nitrate trihydrate ($Cu(NO_3)_2{\cdot}3H_2O$, purity ≥ 99.0%) and zinc oxide (ZnO, purity ≥ 99.0%) were obtained from Sinopharm Chemical Reagent Co., Ltd. (Shanghai, China). Congo red (CR) was purchased from Suzhou Kesaien Biological Technology Co.,

Ltd. (Suzhou, China). Hydrogen peroxide (H_2O_2, 30 wt%) was acquired from Yonghua Chemical Co., Ltd. (Changshu, China).

2.2. Preparation of Rouaite Long Hexagonal Multilayered Nanoplates

Scheme 1 illustrates the ZnO-assisted synthesis of rouaite long hexagonal multilayered nanoplates under continuous ultrasonication. More specifically, 10.1 mg ZnO powder was suspended in 100 mL DI water in a 500 mL beaker and subjected to continuous ultrasonication for 20 min (40 kHz; KQ 300DE, Kunshan Ultrasonic Instrument Co., Ltd., Kunshan, China). At the end of ultrasonication, the ZnO suspension turned into a milk-like color. Afterwards, 150 mL freshly prepared $Cu(NO_3)_2$ solution (0.01 M) was added quickly into the above-mentioned ZnO suspension. The mixed solution was subjected to continuous ultrasonicated for another 30 min. At the end, the bluish-green precipitates were collected by centrifugation, followed by rinsing with DI water and oven-drying at 50 °C for overnight. The yield of rouaite on average is ca. 64% with a standard deviation of ca. 10%, calculated from three parallel batches with the mass of rouaite product of 11.93 mg, 14.23 mg, and 12.14 mg, respectively.

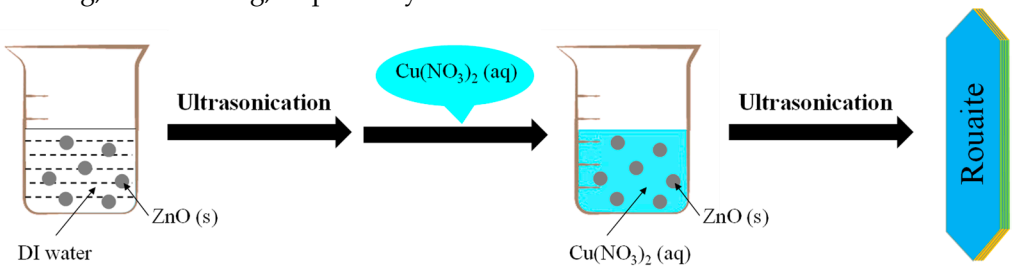

Scheme 1. Schematically illustration of the ZnO-assisted synthesis of rouaite long hexagonal multilayered nanoplates.

2.3. Instrumentation and Characterizations

The sample morphology was characterized using field-emission scanning electron microscopy (FESEM, Hitachi S-4700, operated at 15 kV under high vacuum, Hitachi, Tokyo, Japan) and transmission electron microscopy (TEM, Tecnai G2 20, operated at 200 kV under high vacuum, Tecnai, Madison, WI, USA). The crystal structure and phase purity were confirmed by X'Pert-Pro MPD X-ray diffractometer (Panaco) with monochromatic Cu Kα radiation (λ = 1.54056 Å) at 30 kV and 10 mA, selected area electron diffraction (SAED, integrated in HRTEM, Tecnai G2 F20 S-TWIN, operated at 200 kV under high vacuum). Fourier-transform infrared (FTIR) spectra were acquired using a Nicolet 6700 FTIR spectrometer (Thermo Fisher Scientific, Nieuwegein, The Netherlands) with an ATR method. Raman spectra were carried out on a LabRam HR800 micro-Raman system from Horiba JobinYvon (Palaiseau, France) with a He-Ne laser source (532 nm). The zeta potential was characterized by Zetasizer Nano ZS90 (Malvern, Westborough, MA, USA). The liquid chromatograph-mass spectrometry (LC-MS) analyses were carried out with a mobile (A: 10 mM NH_4HCO_3; B: ACN) and inlet method (3 min (10–95%)-C3-BEH). X-ray photoelectron spectra (XPS) were acquired with a VG Scientific ESCALAB 220i-XL equipped with 300 W Al Kα X-ray radiation source. The C1s binding energy of 284.8 eV was employed as a reference level. The element mapping was carried on an energy dispersive X-ray spectrometer (EDS) integrated in the Hitachi S-4700 FESEM machine.

2.4. Catalytic Assessments

The catalytic performance of wet peroxide oxidation (CWPO) was assessed using Congo red (CR) as a model dye pollutant in water under nearly neutral and ambient conditions (pH 6.76, temperature 20 °C, pressure 1 atm). In a typical experiment, 50 mg of rouaite catalyst was introduced into 100 mL of CR aqueous solution (1×10^{-4} M). Once

the temperature stabilized at 20 °C, 50 μL of fresh hydrogen peroxide (approximately 30 wt%) was added to the solution.

At specified time intervals, UV-vis absorption spectra of the CR reaction solution were recorded using a UV-9000S spectrophotometer (Shanghai Metash Instruments Co., Ltd., Shanghai, China). The concentrations of CR at the initial time (c_0) and at time t (c_t) were determined based on the absorbance at 500 nm—the wavelength at which the CR solution (1×10^{-4} M, pH = 6.76) exhibits its maximum absorbance. Great care was taken during sampling (3 mL each time) to avoid withdrawing any catalyst particles. Nonetheless, each sample was immediately centrifuged to eliminate any potential catalyst residue. The degradation efficiency (η, %) after a certain time period was calculated using the following formula:

$$\eta\ (\%)\ = \frac{c_0 - c_t}{c_0} \times 100\%$$

The total organic carbon (TOC) content of the CR reaction solution was measured at the beginning (t = 0 min) and after 50 min of CWPO treatment using a TOC analyzer (SHIMADZU TOC-L). The TOC removal efficiency (%) was calculated using the following equation:

$$\text{TOC conversion}\ (\%)\ =\ (1\ -\ \frac{\text{TOC}_f}{\text{TOC}_0})\ \times\ 100\%$$

where TOC_0 is the initial TOC content in the CR solution before CWPO treatment (t = 0 min), and TOC_f is the TOC content in the CR solution after CWPO treatment (t = 50 min).

The reusability of the catalyst was assessed through five consecutive catalytic cycles using the same 50 mg batch of rouaite catalyst. In each cycle, 50 μL of fresh hydrogen peroxide (30 wt%) was introduced into 100 mL of a 1×10^{-4} M CR solution. After each run, the rouaite catalyst was recovered from the reaction mixture by centrifugation, thoroughly rinsed with deionized water, and then dried in an oven at 50 °C. Copper leaching from the rouaite catalyst during the CWPO process was evaluated by measuring the Cu^{2+} concentration (mg/L) in the reaction solution using inductively coupled plasma optical emission spectrometry (ICP-OES, PerkinElmer Avio 200, Waltham, MA, USA).

3. Results and Discussion

3.1. Synthesis and Characterization of Rouaite Long Hexagonal Multilayered Nanoplates

The sample prepared from acidic reaction solution (pH = 4.4–4.8) with the assistance of ZnO was firstly characterized by powder X-ray diffraction (XRD). The recorded XRD patterns (Figure 1A,B) match well with the standard pattern of $Cu_2(OH)_3NO_3$ (monoclinic phase, JCPDS No. 75-1779), which is also known as rouaite. No other impurity reflections have been resolved in the XRD pattern, suggesting a high purity of the rouaite sample. The exceptionally strong reflections at 2θ = 12.8° and 25.7° can be assigned to the (001) and (002) reflections, respectively. The series of (00*l*) reflections with regular intervals suggest a multilayered structure of the rouaite sample. It indicates a preferential (00*l*) orientation that is commonly observed for monoclinic-phased 2D nanoplates enclosed with large (00*l*) facets. The crystal structural model given in Figure 1C,D shows the unit cell of monoclinic $Cu_2(OH)_3NO_3$. The interlayer NO_3^- anions are coordinated to the $[Cu_2(OH)_3]^+$ hydroxide layers. The Cu(1)O6 octahedron (in yellow) consists of the central Cu(1) atom with five oxygen (O) atoms from OH^- groups and one oxygen (O) atom from NO_3^- anion. The Cu(2)O6 octahedron (in grey) consists of the central Cu(2) atom with four oxygen (O) atoms from OH^- groups and two oxygen (O) atoms from NO_3^- anions [36].

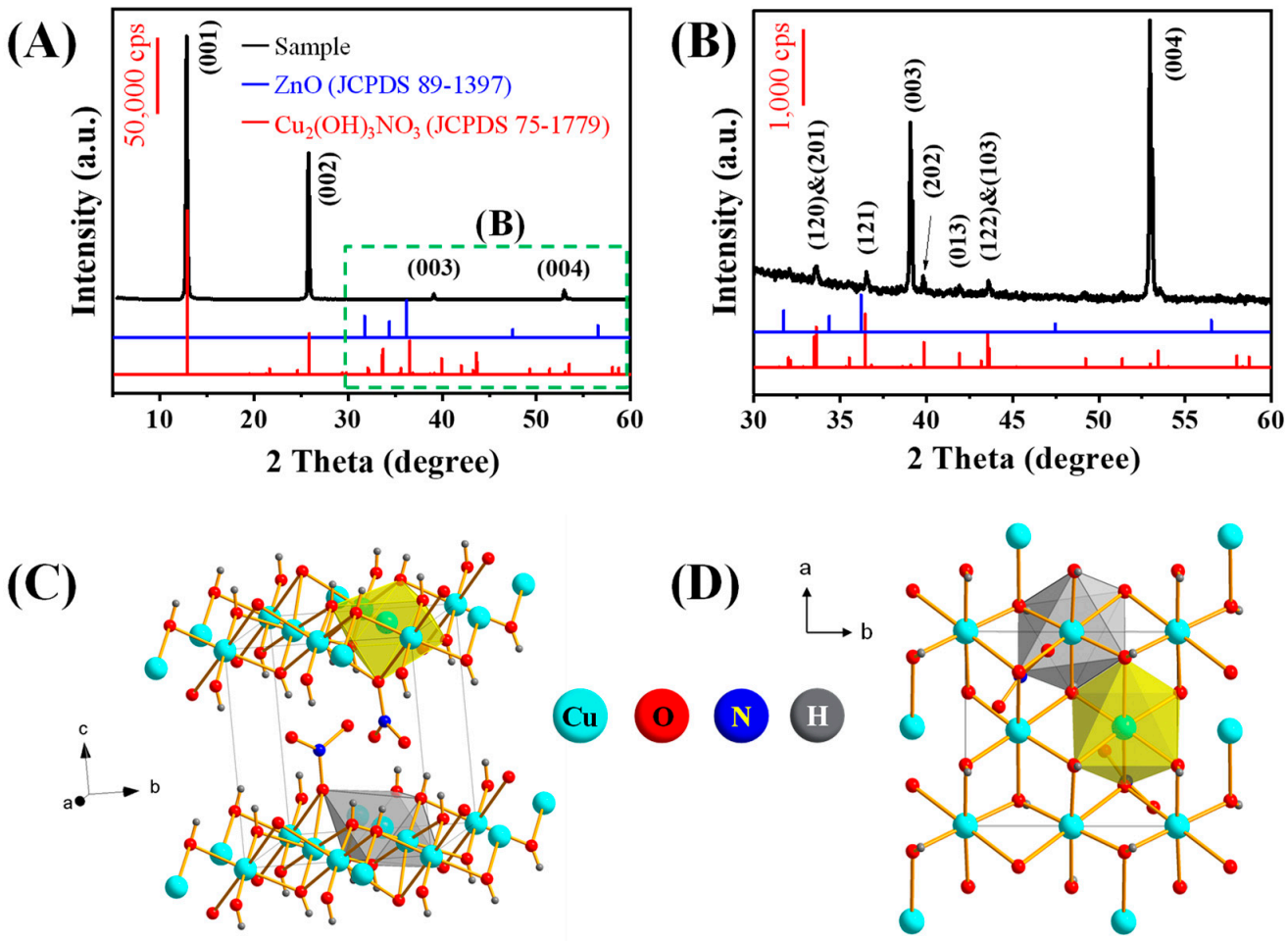

Figure 1. (**A**,**B**) XRD characterization. (**C**,**D**) Unit cell of rouaite ($Cu_2(OH)_3NO_3$, monoclinic phase, space group: P21(4), a = 5.605 Å, b = 6.087 Å, c = 6.929 Å). (**C**) Side view and (**D**) top view of the unit cell.

As a kind of amphoteric oxide, ZnO surfaces are rich in hydroxyl groups [37]. Continuous ultrasonication promotes the hydrolysis of ZnO and a considerable amount of hydroxyl groups were released during hydrolysis. Upon adding $Cu(NO_3)_2$ aqueous solution, the hydroxyl groups react rapidly with $Cu(NO_3)_2$, yielding $Cu_2(OH)_3NO_3$ (rouaite). The total reaction for the ZnO-assisted synthesis of $Cu_2(OH)_3NO_3$ is shown in Equation (1), as follows:

$$4Cu(NO_3)_2(aq) + 3ZnO(s) + 3H_2O(l) \rightarrow 2Cu_2(OH_3)NO_3(s, rouaite) + 3Zn(NO_3)_2(aq) \quad (1)$$

The rouaite sample was further analyzed by SEM and TEM. As shown in Figure 2, the rouaite sample displays a distinctive long hexagonal nanoplate shape. Its multilayered structure can be clearly identified at the nanoplate edge (Figure 2C, denoted by the arrow). The SAED pattern reveals the high single-crystallinity of the rouaite nanoplates (Figure 2D). In the SAED pattern, the (200), (020), (110), and (220) lattice planes can be clearly identified, with the *d*-spacings of $d_{(200)}$ = 2.79 Å, $d_{(020)}$ = 3.05 Å, $d_{(110)}$ = 4.12 Å, and $d_{(220)}$ = 2.06 Å, respectively. The XRD characterization, together with the SEM and TEM characterization, clearly demonstrates the successful synthesis of rouaite long hexagonal multilayered nanoplates.

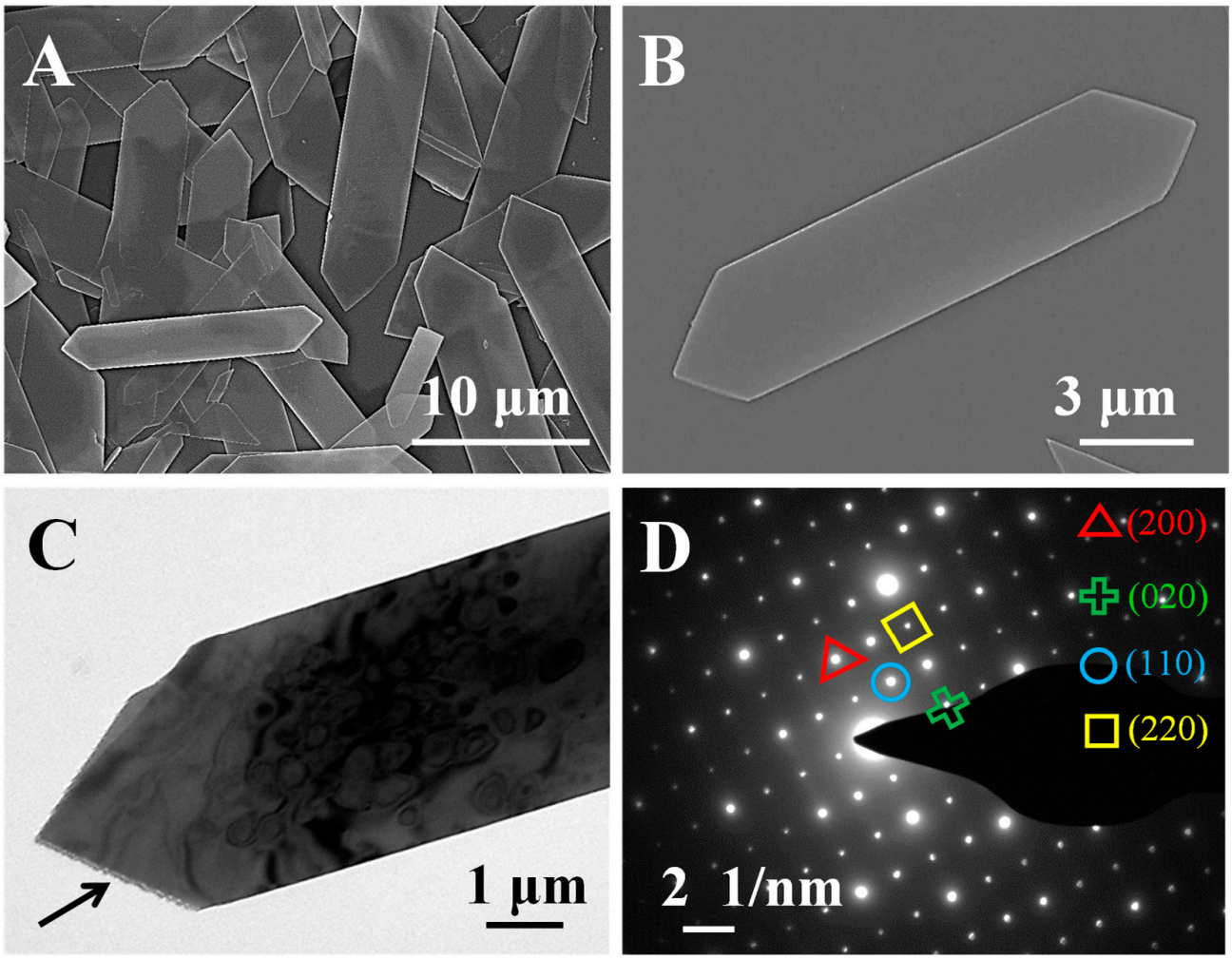

Figure 2. Rouaite long hexagonal multilayered nanoplates. (**A**,**B**) SEM images; (**C**) TEM image; and (**D**) SAED pattern.

The compositional and structural information of the rouaite long hexagonal multilayered nanoplates was further characterized by FTIR (Figure 3). The sharp intense peak at 1046 cm^{-1} belongs to the υ_1(–ONO_2) vibration mode (Figure 3B). The peak at 810 cm^{-1} is assigned to the υ_2(–ONO_2) vibration (Figure 3C). The peaks at 1322 cm^{-1} and 1415 cm^{-1} are corresponding to the υ_3(–ONO_2) vibration (Figure 3D). The peaks located at 709 cm^{-1} and 717 cm^{-1} are ascribed to the υ_4(–ONO_2) vibration. These FTIR vibration bands confirm that the sample contains NO_3^- anions [33]. The H-OH vibration of water molecules has a characteristic peak near 1640 cm^{-1} [38,39]. However, this absorption peak was not present in the FTIR spectrum of rouaite. It suggests that no interlayer water molecules were incorporated in between the $[Cu_2(OH)_3]^+$ hydroxide layers. The peaks at 3543 cm^{-1} and 3410 cm^{-1} belong to the typical hydroxyl stretching vibration [38,39], indicating that the rouaite sample contains OH^- groups. The peaks at 874, 773, and 668 cm^{-1} are attributable to the bending of Cu–O-H bonds that are depending on the degree of hydrogen bonding [33,40].

Figure 4 shows the normal Raman spectra of the rouaite long hexagonal multilayered nanoplates. The intense and fine peak at 1050 cm^{-1} can be assigned to the υ_1(–ONO_2) vibration (Figure 4A). The band at 3550 cm^{-1} and the shoulder band at the right side are attributed to the stretching vibration of hydroxyl groups (Figure 4B). The bands at 1322, 1361, and 1426 cm^{-1} are associated with the υ_3(–ONO_2) vibration (Figure 4C). The band at 798 cm^{-1} is corresponding to the overlapping of the υ_2(–ONO_2) vibration and the Cu-O-H bending vibration (Figure 4D). The band at 718 cm^{-1} is ascribed to the υ_4(–ONO_2)

vibration. The bands at 880 and 668 cm^{-1} are the bending vibrations generated by the hydrogen bonding in Cu–O-H (Figure 4D). The three bands at 508, 462, and 413 cm^{-1} can be assigned to the OH deformation mode in the $[Cu_2(OH)_3]^+$ hydroxide layers (Figure 4E) [41]. The band at 336 cm^{-1} is attributable to the O—H—O hydrogen bonds (Figure 4E) [41]. Based on the above information, the Raman characterization further demonstrates that the chemical formula of the samples is $Cu_2(OH)_3NO_3$, in good agreement with the XRD and FTIR characterizations.

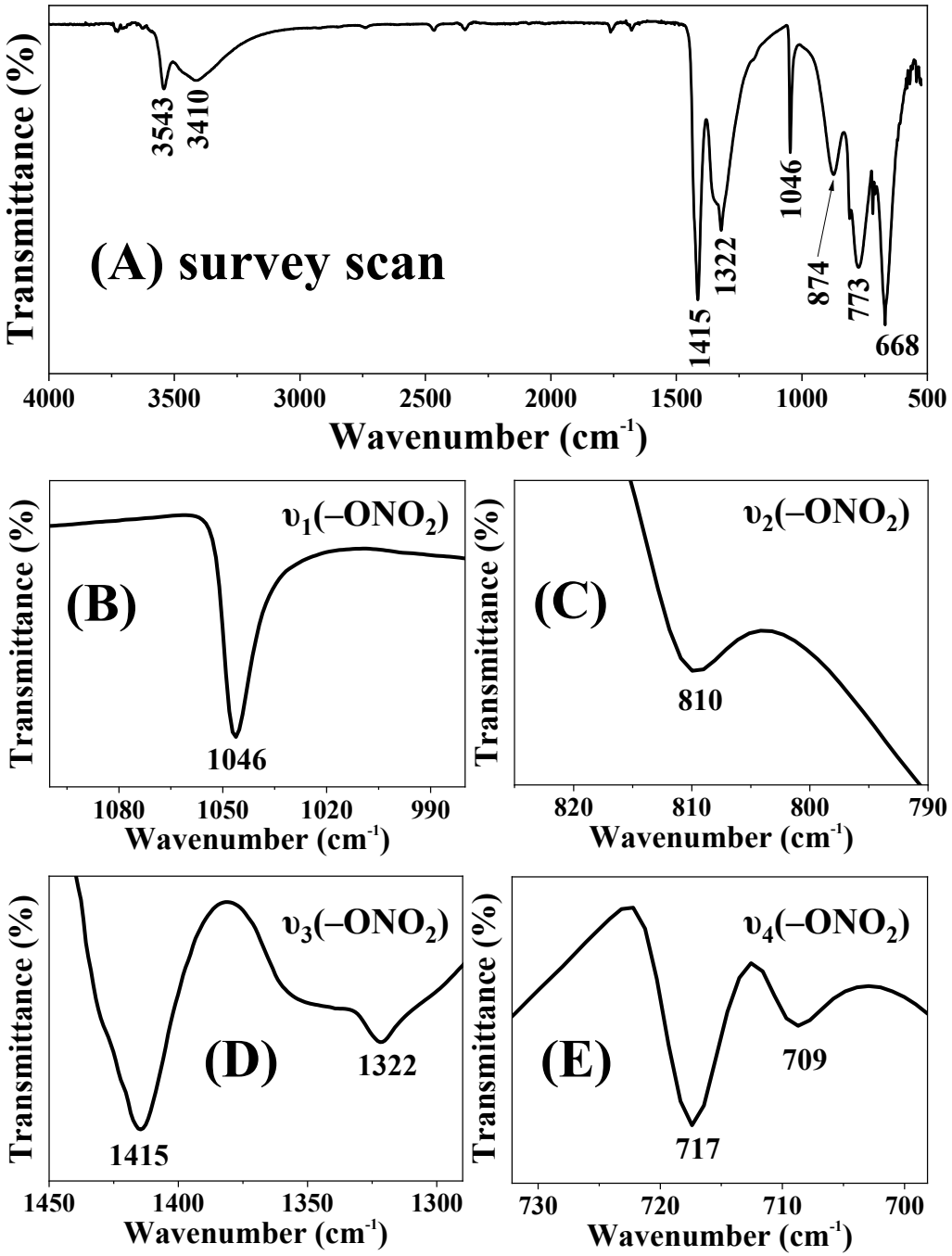

Figure 3. FTIR characterization of the rouaite long hexagonal multilayered nanoplates. (**A**) Survey scan; and (**B**–**E**) close-up views of the $–ONO_2$ vibrations.

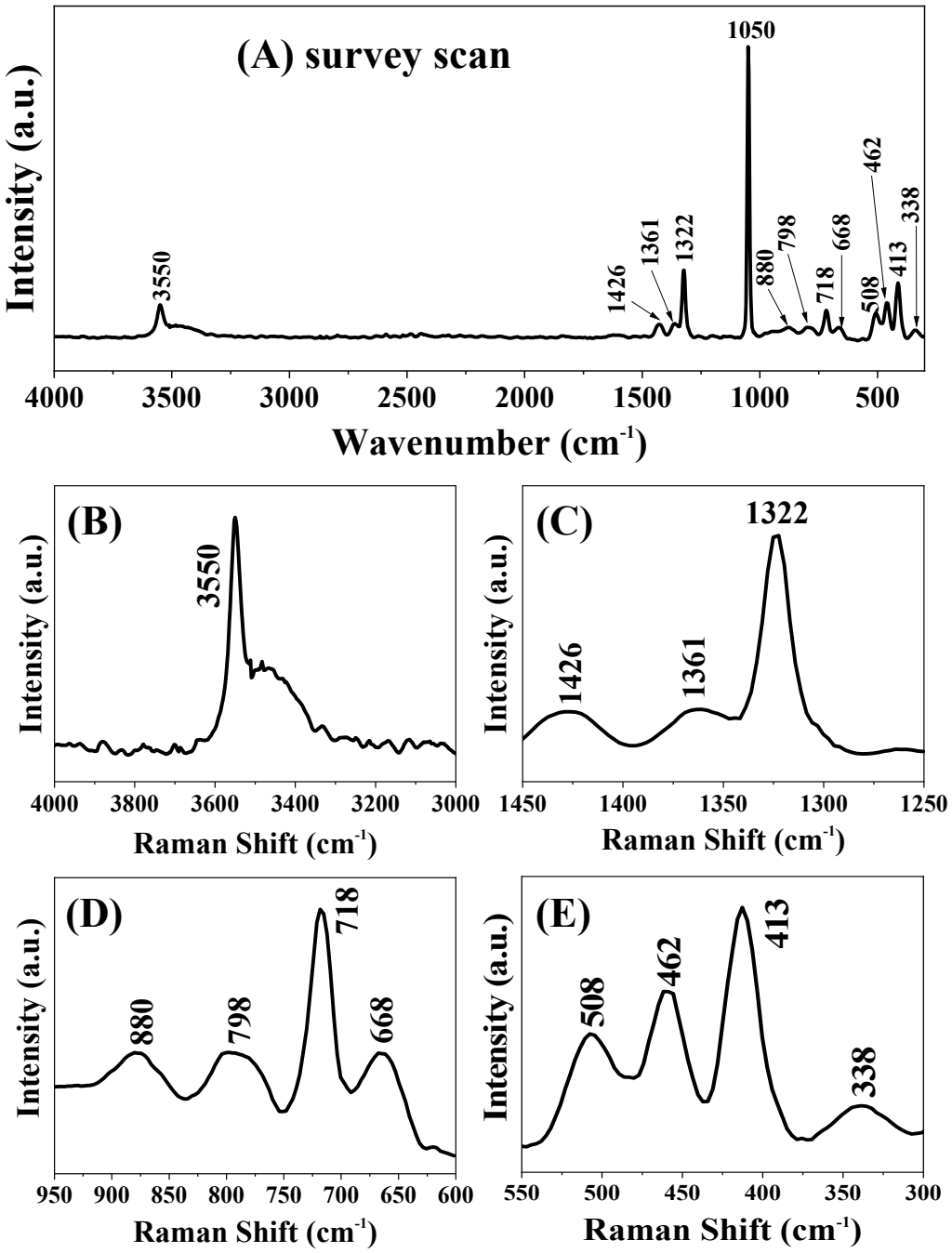

Figure 4. Normal Raman spectra of the rouaite long hexagonal multilayered nanoplates. (**A**) Survey scan; and (**B**–**E**) close-up views of different spectral regions.

The rouaite long hexagonal multilayered nanoplates were further characterized by X-ray photoelectron spectroscopy (XPS) to investigate the valence state of elements and the surface composition (Figure 5). The binding energy of Cu $2p_{3/2}$ and Cu $2p_{1/2}$ is measured to be 935.3 and 955.1 eV, respectively (Figure 5B). According to the literature [42,43], the binding energy of Zn $2p_{1/2}$ and Zn $2p_{3/2}$ locates at 1044.1 and 1022.0 eV, respectively. The XPS scan did not resolve any peak of Zn $2p_{1/2}$ and Zn $2p_{3/2}$ (Figure 5C). The result indicates that ZnO has been completely consumed during the synthesis process. It further confirms the high purity of the rouaite sample, consistent with the XRD results. In the O 1s spectrum (Figure 5D), the peaks at 532.1 eV and 532.7 eV correspond to the O 1s peaks in OH^- and NO_3^-, respectively. Figure 5E shows that the N 1s peak is observed at 406.8 eV, consistent with the literature.

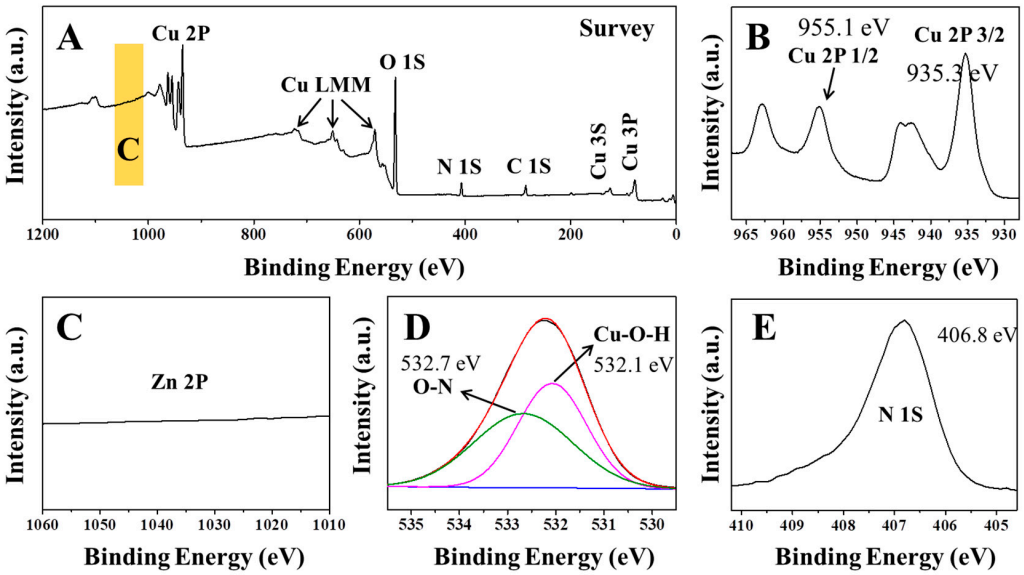

Figure 5. XPS spectra of the rouaite long hexagonal multilayered nanoplates. (**A**) Survey scan; (**B**) Cu 2p; (**C**) Zn 2p; (**D**) O1s; and (**E**) N 1s.

3.2. Catalytic Wet Peroxide Oxidation of Congo Red over Rouaite Nanoplates

The rouaite long hexagonal multilayered nanoplates were applied as the heterogeneous catalyst for catalytic wet peroxide oxidation (CWPO) of the azo-dye Congo red (CR) under near-neutral (pH = 6.76) and ambient conditions (T = 20 °C, p = 1 atm), employing H_2O_2 as the oxidant. As depicted by the black plot in Figure 6A, CR was barely decolorized in the presence of H_2O_2 only. When 50 mg rouaite catalyst together with 50 µL H_2O_2 were added into the CR solution, as can be seen from the CWPO plot (the blue plot, Figure 6A), the CR decolorization efficiency was dramatically enhanced. The decolorization efficiency was 62.4% at 10 min and steadily increased to 96.3% in 50 min, without needing an increased temperature and/or an acidic pH (pH ≈ 3), as is commonly done in the CWPO process for improved degradation efficiency [31,32]. A distinct plateau appeared after 35 min in the CWPO plot (Figure 6A). This plateau is commonly observed in the oxidative dye degradation process, typically associated with the formation of ultimate degradation products, such as light-weight carboxylic acids [44].

Figure 6B displays the kinetic plot of $(1 - c_t/c_0)/t \sim 1/t^{1/2}$ for CR decolorization, with a high linear correlation coefficient of $r^2 \sim 0.9988$. The good linear fitting indicates that the decolorization kinetics can be fitted well using the following parabolic diffusion model [45,46]: $(1 - C_t/C_0)/t = k/t^{1/2} + a$. The apparent rate constant (k) is calculated to be 0.283 L·mol^{-1}. Our group has reported the flowerlike nanoplate superstructures of brochantite ($Cu_4(OH)_6SO_4$) for CWPO decolorization of CR [30]. Under the same catalytic condition (i.e., catalyst loading: 50 mg, H_2O_2 dosage: 50 µL, and reaction time: 30 min), the CR decolorization efficiency was 82.6% in the presence of the brochantite catalyst. The rouaite catalyst exhibited improved catalytic performance comparing to the brochantite catalyst. The dye decolorization efficiency reached 96.3% in 50 min under near-neutral (pH = 6.76, H_2O_2 = 50 µL) and ambient conditions (T = 20 °C, p = 1 atm).

$$C_{32}H_{22}N_6Na_2O_6S_2 + 76H_2O_2 \rightarrow 32CO_2\uparrow + 3N_2\uparrow + 2Na^+ + 2H^+ + 2SO_4{}^{2-} + 86H_2O \quad (2)$$

Equation (2) shows the reaction equation between CR ($C_{32}H_{22}N_6Na_2O_6S_2$) and H_2O_2 towards the complete mineralization of CR. The theoretical stoichiometric H_2O_2/CR ratio is 76. Figure S1 shows the survey for the optimal dosage of H_2O_2. The optimal H_2O_2 dosage in our study is 50 µL, which is ca. 64% of the theoretical stoichiometric

amount. Under the optimal H_2O_2 dosage, the CR decolorization efficiency reached 96.3% at 50 min. Nevertheless, the rouaite catalyst still exhibited high catalytic activity under lower H_2O_2 dosages. The CR decolorization efficiency reached 92% at 50 min under 10 µL H_2O_2 dosage (ca. 13% of the theoretical stoichiometric amount). Note the following: The theoretical stoichiometric amount refers to the dosage of H_2O_2 required for the complete oxidation of CR, if only decolorization is considered, it is sufficient to destroy the important chromophoric groups, so much less H_2O_2 is needed. The catalyst-to-dye mass ratio in our study (7:1) is also lower than that used in most literature reports [28,47]. Nevertheless, the excellent catalytic performance of the rouaite catalyst is apparently superior to most of the reported catalysts (see Table S1).

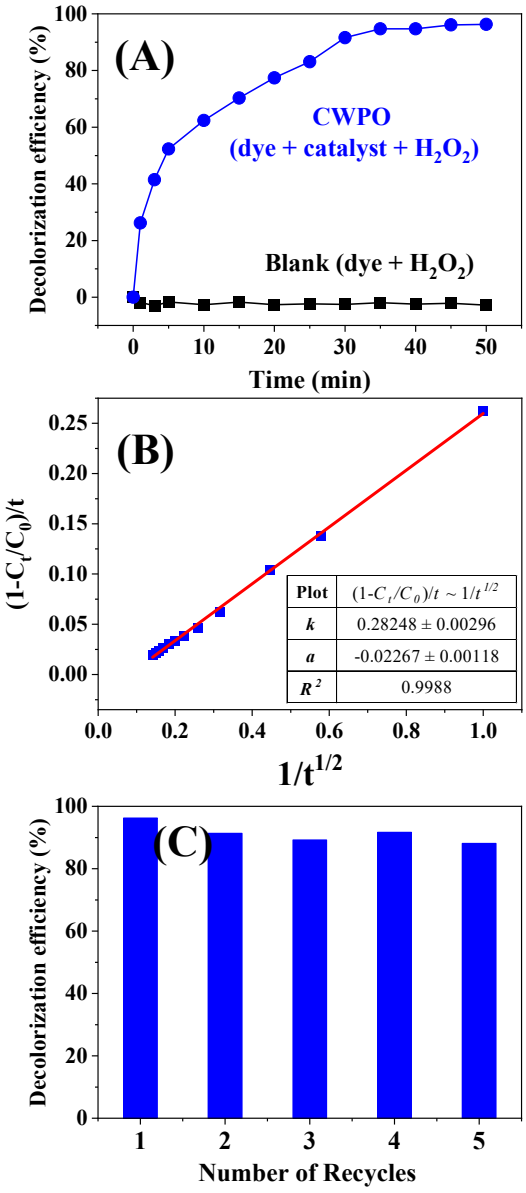

Figure 6. CR decolorization via CWPO process. (**A**) Comparison of the CR decolorization efficiency under different catalytic conditions: CWPO (blue): in the presence of both the rouaite catalyst and H_2O_2. Blank (black): in the presence of H_2O_2 only. (**B**) The kinetic plot of $(1 - c_t/c_0)/t \sim 1/t^{1/2}$ for the CWPO decolorization kinetics. (**C**) Evaluation for the reusability of the rouaite catalyst. The histogram displays the CR decolorization efficiency assessed at 50 min in all five successive cyclic runs. Conditions for each catalytic run: catalyst loading: 50 mg. H_2O_2 dosage: 50 µL. CR solution: 100 mL, 1×10^{-4} M. pH = 6.76. T = 20 °C. p = 1 atm.

Reusability and stability are crucial parameters to evaluate the catalytic performance of a catalyst in real-scale practical utilization. As shown in Figure 6C, the rouaite catalyst retained the initial catalytic activity without obvious decay after 5 successive cyclic runs. To further assess the catalyst stability, the Cu leaching was characterized as the Cu^{2+} concentration (mg/L) in the reaction solution. As can be seen in Table S2, the Cu^{2+} concentration in the reaction solution was low (<2.65 mg/L) throughout the CWPO process, indicating a negligible Cu leaching from the rouaite catalyst. It is noteworthy that the catalytic CWPO process in our study was carried out under near-neutral (pH = 6.76) and ambient conditions (T = 20 °C, p = 1 atm), with low H_2O_2 dosage (only 50 μL) and without necessary for an increased temperature and/or an acidic pH (pH ≈ 3) as is commonly done in literature-reported CWPO processes for improved degradation efficiency [31,32]. The negligible Cu leaching from the rouaite catalyst was mainly attributed to the moderate catalytic conditions, especially the near-neutral condition (pH = 6.76). Negligible leaching of metals from the catalyst has also been reported in the CWPO process carried out under near-neutral conditions [28,40].

The stable structure of rouaite may have also attributed to the negligible Cu leaching. Rouaite is a typical monoclinic crystal with a characteristic layered structure (see Figure 1C,D). In the $[Cu_2(OH)_3]^+$ hydroxide layers, each copper ion (Cu^{2+}) is coordinated with six oxygen (O) atoms, forming stable octahedra. In addition to the moderate catalytic conditions, the structure of rouaite with stable CuO6 octahedra in the $[Cu_2(OH)_3]^+$ hydroxide layers further ensure the negligible leaching of Cu. The negligible leaching of Cu from rouaite is further supported by the SEM characterization. As revealed by the SEM image (see Figure S2), the long hexagonal nanoplate morphology of the rouaite catalyst was well retained after 5 successive cyclic runs. Figure S3 shows the XRD characterization of the rouaite catalyst after 5 successive cyclic runs. All the reflections can be indexed to $Cu_2(OH)_3NO_3$ (JCPDS 75-1779), confirming that no copper hydroxides or oxides have been formed in the CWPO process.

The CWPO catalytic efficiency is closely correlated with the temperature and the pH value of the reaction solution. Increasing the reaction temperature and/or decreasing the pH value (pH = 2~3) has been proven to be effective for boosting the catalytic efficiency [31,32]. It is noteworthy that in our study the high catalytic efficiency for CR decolorization (96.3% in 50 min) was achieved under near-neutral (pH = 6.76) and ambient conditions (T = 20 °C, p = 1 atm), without increasing the temperature and/or decreasing the pH value. Therefore, the CWPO process in our study allows us to technically replicate at most the real-scale applications in practice. Despite that improved dye degradation efficiency is achievable at higher temperatures, it would also cause more energy consumption. Moreover, it is not a practical strategy to employ non-room-temperature conditions in real-scale applications. Similarly, it is both challenging and economically unfeasible to adjust an acidic pH for improved CWPO efficiency. An acidic pH condition would cause severe leaching of metals from the catalyst [48].

It is well-known that the hydroxyl radicals ($HO^{\bullet}$) are the main reactive oxidative species (ROS) in the CWPO process. To mechanically elucidate the catalytic oxidation of CR in the CWPO process, the trapping tests were carried out by utilizing isopropanol as the hydroxyl radical scavenger [49]. As can be seen in Figure 7, the CR decolorization efficiency at 25 min sharply decreased from 83.1% to 38.6% in the presence of isopropanol, which was just a little higher than the 31.2% removal efficiency through physical adsorption. The trapping test results confirm that the hydroxyl radicals ($HO^{\bullet}$) are the main ROS in the CWPO reactions. The CWPO performance of copper-based catalysts depends on the Cu^{2+}/Cu^{+} cyclic conversion [50]. More specifically, Cu^{2+} and Cu^{+} cations react with H_2O_2 and create the highly active hydroxyl radicals (Equations (3)–(5)). Eventually, the hydroxyl

radical ($HO^{\bullet}$) with strong oxidative ability destructively degrade the dye molecules (R-H) into small nontoxic molecules (Equation (6)).

$$Cu^{2+} + H_2O_2 \rightarrow CuOOH^{+} + H^{+} \quad (3)$$

$$CuOOH^{+} \rightarrow HOO^{\bullet} + Cu^{+} \quad (4)$$

$$Cu^{+} + H_2O_2 \rightarrow Cu^{2+} + HO^{\bullet} + OH^{-} \quad (5)$$

$$R\text{–}H + HO^{\bullet} \rightarrow \text{degradation products} \quad (6)$$

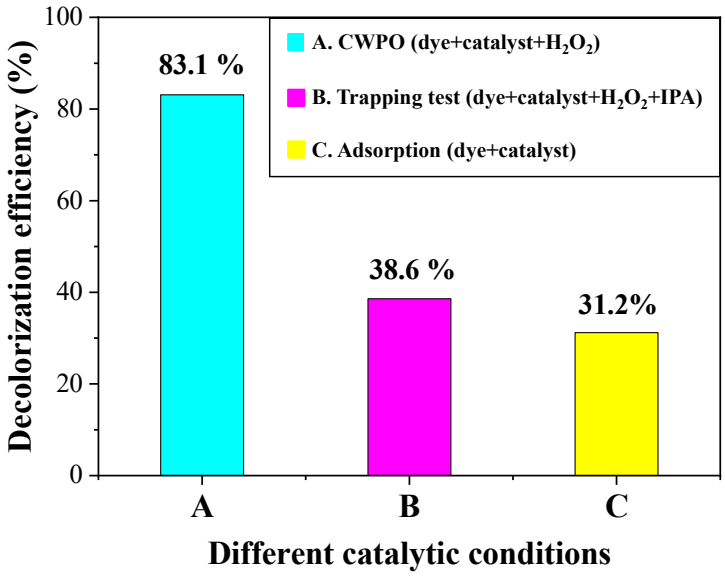

Figure 7. Comparison of the CR decolorization efficiency under different catalytic conditions: (**A**) in the CWPO process, (**B**) in the trapping test, and (**C**) in the physical adsorption process. The CR decolorization efficiency was assessed at 25 min in all cases. Catalyst loading: 50 mg. H_2O_2 dosage: 50 μL. CR solution: 100 mL, 1×10^{-4} M, pH =6.76. T = 20 °C. p = 1 atm.

To further disclose the influence of H_2O_2 on CR decolorization, the controlled catalytic reaction was conducted by adding the rouaite catalyst only into the CR solution but without H_2O_2. As can be seen in Figure S4A, the CR removal efficiency evaluated at 10 min dropped sharply from 62.4% to 27.6% in the absence of H_2O_2. The CR decolorization efficiency reached 96.3% in 50 min in the CWPO process when both the rouaite catalyst and H_2O_2 were added into the CR solution, while the CR removal efficiency was only 33.6% when only the rouaite catalyst was added into the CR solution. In this case, the CR removal efficiency is mainly attributed to physical adsorption. The physical adsorption reached saturation in the first run. As a result, the CR removal efficiency in the following cyclic runs without H_2O_2 was negligible (see the red histogram, Figure S4B). In the CWPO process, by contrast, the CR degradation retained the initial efficiency without obvious decay after 5 successive cyclic runs (see the blue histogram, Figure S4B). Figure S4C shows the color change of the rouaite catalyst under different catalytic conditions. When both the rouaite catalyst and H_2O_2 were added into the CR solution, the initially bluish-green rouaite catalyst turned to grayish-green after the CWPO process (top panel, Figure S4C). When only the rouaite catalyst was added into the CR solution, the rouaite catalyst became red after reaching balance with the CR solution (bottom panel, Figure S4C). The color change further confirms that a physical adsorption process instead of a catalytic degradation process has occurred when only the rouaite catalyst was added into the CR solution.

We have also examined the zeta potential of the rouaite catalyst. As shown in Figure S5, the zeta potential is +36.0 mV, which is attributable to the positively charged $[Cu_2(OH)_3]^{+}$

hydroxide layers. The anionic CR dye can be easily adsorbed on the positively charged surface of rouaite catalyst. In short, the positively charged surface together with its large surface area and 2D multilayer structure ensures the superior adsorption capacity of the rouaite catalyst towards the anionic CR dye. It is reasonable to believe that the excellent CWPO catalytic performance of the rouaite catalyst is favored by its superior CR adsorption capacity.

To further mechanically elucidate the CWPO process for CR decolorization, we have conducted EDS element mapping for (1) the as-prepared rouaite catalyst, (2) the rouaite catalyst after the CR adsorption in the absence of H_2O_2, and (3) the rouaite catalyst after CR decolorization in the presence of H_2O_2. The as-prepared rouaite catalyst does not contain the sulfur (S) element (see Figure S6A). The copper (Cu) content in the rouaite catalyst is 51.48%, close to the theoretical Cu content in $Cu_2(OH)_3NO_3$ (52.93%). After CR adsorption in the absence of H_2O_2, the S element from the sulfate groups of CR was detected in the rouaite catalyst (Figure S6B). The rouaite catalyst after CR decolorization also contained the S element (Figure S6C).

To identify the degradation intermediates, we have carried out a liquid chromatograph-mass spectrometry (LC-MS) analysis of the CR reaction solution before and after CWPO treatment (Figures S7 and S8). As can be seen from the LC-MS analysis for the CR reaction solution before CWPO treatment shown in Figure S7A, two kinds of CR anions were found. CR anions carrying with two negative charges (i) were found in the test, with a mass-to-charge ratio of 325.1. CR anions carrying with one negative charge (ii) also were found in the test, with an m/z ratio of 651.7. Upon reacting with the hydroxyl radicals ($HO^{\bullet}$), the azo (—N=N—) bonds will be cleaved firstly. Accordingly, the two absorption bands associated with the —N=N— bonds (that is, the π-π^* transition band at 340 nm and the n-π^* transition band at 500 nm) disappeared gradually from the UV-vis absorption spectra (see Figure S9). The UV-vis absorption results confirmed the complete cleavage of the —N=N— bonds.

The hydroxyl radicals ($HO^{\bullet}$) will continuously attack the aromatic groups, leading to the further cleavage of S—C and N—C bonds on aromatic rings, the hydroxylation and/or aldehydation of aromatic groups, the opening and the following oxidation of aromatic rings, etc. Consequently, a set of carboxylic acids with different m/z ratios will be formed. Figure S8A,B show the LC-MS analysis of the CR solution after the CWPO treatment. Figure S8C lists the possible degradation intermediates with the m/z ratios resolved in the LC-MS analysis. The LC-MS results are consistent with the literature on the oxidative degradation of CR [47,51]. In the UV-vis absorption spectra (please kindly see Figure S9), the absorption band centered at 370 nm are attributable to the carboxylic acid degradation intermediates. The weak absorption at around 280 nm is attributable to a small amount of nitronaphthalene degradation intermediates. The UV-vis absorption results (Figure S9) agree with the LC-MS results (Figure S8).

The TOC content in the CR reaction solution was analyzed before (t = 0 min) and after (t = 50 min) CWPO treatment. The TOC conversion efficiency was 57.23% at 50 min (Figure S10). The TOC content in the CR reaction solution after CWPO treatment is mainly attributed to the light-weight carboxylic acid degradation intermediates. For the big CR molecules with a complex conjugated structure, the degradation pathway is a multi-step process and involves the formation of a set of degradation intermediates, as revealed by the LC-MS analysis (see Figure S8). It takes a longer time for complete mineralization of the degradation intermediates. This rationalizes that the TOC conversion efficiency is reasonably lower than the high decolorization efficiency assessed at the same reaction time under the same catalytic conditions.

4. Conclusions

In conclusion, the present work has reported the ZnO-assisted synthesis of rouaite ($Cu_2(OH)_3NO_3$) long hexagonal multilayered nanoplates and their application as the heterogeneous catalyst for catalytic wet peroxide oxidation (CWPO) of CR. Rouaite long hexagonal multilayered nanoplates with high purity and high crystallinity have been prepared from acidic reaction solution (pH = 4.4–4.8) with the assistance of ZnO under continuous ultrasonication conditions. The mechanical ultrasonication promotes the hydrolysis of ZnO. The in situ homogeneous release of hydroxide anions (OH^-) upon the hydrolysis of ZnO is the key for the successful synthesis of rouaite from the acidic $Cu(NO_3)_2$ solution, remarkably distinctive from the literature, in which rouaite was usually prepared by precipitation from alkaline solution with pH > 11. The rouaite long hexagonal multilayer nanoplates show superior catalytic activity for CR decolorization via CWPO. The CR decolorization efficiency reached 96.3% in 50 min under near-neutral (pH = 6.76) and ambient conditions (T = 20 °C, p = 1 atm), without the need for increasing the temperature or decreasing the pH value. The excellent catalytic activity of rouaite catalyst was attributed by the intrinsic Cu^{2+}/Cu^{+} cycling activity as well as the multilayered structure, the positively charged surface, and the large surface area associated with the long nanoplate morphology.

Supplementary Materials: The following supporting information can be downloaded at https://www.mdpi.com/article/10.3390/cryst15080710/s1: Figure S1: Survey for the optimal dosage of H_2O_2, Table S1: comparison of the CR degradation efficiency in our study with that in literature reports, Table S2: the assessment of Cu leaching (mg/L) from the rouaite catalyst, Figures S2 and S3: SEM and XRD characterizations of the rouaite catalyst after five cyclic runs, Figure S4: comparison of the CR removal efficiency under different catalytic conditions, Figure S5: zeta potential of the rouaite catalyst, Figure S6: EDS element mappings, Figures S7 and S8: LC-MS analysis, Figure S9: UV-vis absorption spectra of the CR solution during the CWPO reaction, Figure S10: TOC analysis after CWPO treatment (PDF).

Author Contributions: Conceptualization, J.H.W.; methodology, J.H.W.; validation, J.H.W.; formal analysis, J.H.W.; investigation, G.Y.Z., J.G. and J.H.W.; resources, J.H.W.; data curation, J.H.W.; writing—original draft, G.Y.Z. and J.H.W., writing—review and editing, G.Y.Z. and J.H.W.; visualization, J.H.W.; supervision, J.H.W.; project administration, J.H.W. All authors have read and agreed to the published version of the manuscript.

Funding: We are thankful for the financial support from the National Natural Science Foundation of China (Project 21373145), the College of Chemistry, Chemical Engineering and Materials Science, Suzhou University, China, the Priority Academic Program Development of Jiangsu Higher Education Institutions (PAPD).

Data Availability Statement: The original contributions presented in this study are included in the article/Supplementary Materials. Further inquiries can be directed to the corresponding authors.

Conflicts of Interest: The authors declare no conflicts of interest.

References

1. Li, Y.L.; Ai, J.F.; Chen, Z.C.; Wang, H.L.; Zhu, Z.H.; Liang, F.P.; Zou, H.H. Multiple Strategies Enhance the ROS of Metal–Organic Frameworks for Energy-Efficient Photocatalytic Water Purification and Sterilization. *ACS Mater. Lett.* **2023**, *5*, 1317–1331. [CrossRef]
2. Ahmad, I.; Aftab, M.A.; Fatima, A.; Mekkey, S.D.; Melhi, S.; Ikram, S. A comprehensive review on the advancement of transition metals incorporated on functional magnetic nanocomposites for the catalytic reduction and photocatalytic degradation of organic pollutants. *Coord. Chem. Rev.* **2024**, *514*, 215904. [CrossRef]
3. Schwarzenbach, R.P.; Escher, B.I.; Fenner, K.; Hofstetter, T.B.; Johnson, C.A.; von Gunten, U.; Wehrli, B. The Challenge of Micropollutants in Aquatic Systems. *Science* **2006**, *313*, 1072–1077. [CrossRef]
4. Chung, K.T. Azo Dyes and Human Health: A Review. *J. Environ. Sci. Health Part C* **2016**, *34*, 233–261. [CrossRef] [PubMed]

5. Lee, S.J.; Han, X.G.; Men, X.; Oh, G.; Choi, S.I.; Lee, O.H. Improvement of analytical method for three azo dyes in processed milk and cheese using HPLC-PDA. *Food Chem. X* **2023**, *18*, 100713. [CrossRef]
6. Joshy, D.; Chakko, S.; Ismail, Y.A.; Periyat, P. Surface basicity mediated rapid and selective adsorptive removal of Congo red over nanocrystalline mesoporous CeO_2. *Nanoscale Adv.* **2021**, *3*, 6704–6718. [CrossRef]
7. Castillo-Cervantes, J.N.; Gómora-Herrera, D.R.; Navarrete-Bolaños, J.; Likhanova, N.V.; Olivares-Xometl, O.; Lijanova, I.V. A complete in-situ analysis of UV–vis and 2D-FTIR spectra of the molecular interaction between RO16 (azo dye) and synthesized ammonium-based ionic liquids. *Sep. Purif. Technol.* **2021**, *254*, 117652. [CrossRef]
8. Gu, S.G.; Ma, Y.; Zhang, T.; Yang, Y.T.; Xu, Y.L.; Li, J. MXene Nanosheet Tailored Bioinspired Modification of a Nanofiltration Membrane for Dye/Salt Separation. *ACS EST Water* **2023**, *3*, 1756–1766. [CrossRef]
9. Jia, Y.H.; Ding, L.; Ren, P.Y.; Zhong, M.Y.; Ma, J.Y.; Fan, X.R. Performances and Mechanism of Methyl Orange and Congo Red Adsorbed on the Magnetic Ion-Exchange Resin. *J. Chem. Eng. Data* **2020**, *65*, 725–736. [CrossRef]
10. Ahmed, M.B.; Zhou, J.L.; Ngo, H.H.; Guo, W.S.; Thomaidis, N.S.; Xu, J. Progress in the biological and chemical treatment technologies for emerging contaminant removal from wastewater: A critical review. *J. Hazard. Mater.* **2017**, *323*, 274–298. [CrossRef]
11. Yang, Z.Z.; Zhang, C.; Zeng, G.M.; Tan, X.F.; Wang, H.; Huang, D.L.; Yang, K.H.; Wei, J.J.; Ma, C.; Nie, K. Design and engineering of layered double hydroxide based catalysts for water depollution by advanced oxidation processes: A review. *J. Mater. Chem. A* **2020**, *8*, 4141–4173. [CrossRef]
12. Zhong, H.; Qin, Q.; Wang, Z.; Zhang, H.; Qiu, Y.; Yin, D.; Liu, X.; Zhu, Z. Insight into Peroxymonosulfate Activation Catalyzed by Fe/Mn Bimetallic-Loaded In Situ Nitrogen-Doped Biochar: The Critical Role of Singlet Oxygen and Superoxide Radicals. *Langmuir* **2025**, *41*, 7089–7100. [CrossRef] [PubMed]
13. Xu, W.; Zhang, Y.; Xu, X.; Chen, J. Construction of Mo-Based p-n Heterojunction with Enhanced Oxidase-Mimic Activity for AOPs and Antibiofouling. *Inorg. Chem.* **2023**, *62*, 14773–14781. [CrossRef] [PubMed]
14. Wang, Y.P.; Liu, Y.; Zhang, H.Y.; Duan, X.G.; Ma, J.; Sun, H.Q.; Tian, W.J.; Wang, S.B. Carbonaceous materials in structural dimensions for advanced oxidation processes. *Chem. Soc. Rev.* **2025**, *54*, 2436–2482. [CrossRef]
15. Guo, J.R.; Gao, B.Y.; Li, Q.; Wang, S.B.; Shang, Y.N.; Duan, X.G.; Xu, X. Size-Dependent Catalysis in Fenton-like Chemistry: From Nanoparticles to Single Atoms. *Adv. Mater.* **2024**, *36*, 2403965. [CrossRef]
16. Wang, Y.H.; Sun, Y.L.; Wang, R.Y.; Gao, M.C.; Xin, Y.J.; Zhang, G.S.; Xu, P.; Ma, D. Activation of peroxymonosulfate with cobalt embedded in layered δ-MnO_2 for degradation of dimethyl phthalate: Mechanisms, degradation pathway, and DFT calculation. *J. Hazard. Mater.* **2023**, *451*, 130901. [CrossRef]
17. Kim, J.; Song, O.; Cho, Y.S.; Jung, M.; Rhee, D.; Kang, J. Revisiting Solution-Based Processing of van der Waals Layered Materials for Electronics. *ACS Mater. Au* **2022**, *2*, 382–393. [CrossRef]
18. Yuan, S.G.; Pang, S.Y.; Hao, J.H. 2D Transition Metal Dichalcogenides, Carbides, Nitrides, and Their Applications in Supercapacitors and Electrocatalytic Hydrogen Evolution Reaction. *Appl. Phys. Rev.* **2020**, *7*, 021304. [CrossRef]
19. Cao, Y.H.; Li, B.; Zhong, G.Y.; Li, Y.H.; Wang, H.J.; Yu, H.; Peng, F. Catalytic wet air oxidation of phenol over carbon nanotubes: Synergistic effect of carboxyl groups and edge carbons. *Carbon* **2018**, *133*, 464–473. [CrossRef]
20. Khan, Z.U.H.; Gul, N.S.; Sabahat, S.; Sun, J.Y.; Tahir, K.; Shah, N.S.; Muhammad, N.; Rahim, A.; Imran, M.; Iqbal, J.; et al. Removal of organic pollutants through hydroxyl radical-based advanced oxidation processes. *Ecotox. Environ. Safe* **2023**, *267*, 115564. [CrossRef] [PubMed]
21. Yu, D.Y.; Xu, L.C.; Fu, K.X.; Liu, X.; Wang, S.L.; Wu, M.H.; Lu, W.Y.; Lv, C.Y.; Luo, J.M. Electronic structure modulation of iron sites with fluorine coordination enables ultra-effective H_2O_2 activation. *Nat. Commun.* **2024**, *15*, 2241. [CrossRef] [PubMed]
22. Wang, Y.M.; Wei, H.Z.; Zhao, Y.; Sun, W.J.; Sun, C.L. Low temperature modified sludge-derived carbon catalysts for efficient catalytic wet peroxide oxidation of m-cresol. *Green Chem.* **2017**, *19*, 1362–1370. [CrossRef]
23. Ou, X.X.; Pilitsis, F.; Xu, N.H.; Taylor, S.F.R.; Warren, J.; Garforth, A.; Zhang, J.S.; Hardacre, C.; Jiao, Y.L.; Fan, X.L. On developing ferrisilicate catalysts supported on silicon carbide (SiC) foam catalysts for continuous catalytic wet peroxide oxidation (CWPO) reactions. *Catal. Today* **2020**, *356*, 631–640. [CrossRef]
24. Choi, H.; Yanagita, M.; Teramoto, Y.; Takano, T. Preparation of hemin-bound chitosan flakes and their dye decolorizing ability. *Int. J. Biol. Macromol.* **2025**, *307*, 141952. [CrossRef]
25. El-Eswed, B.; Albawarshi, Y. Utilization of encapsulating, anti-oxidizing, and green capping features of metakaolin based geopolymers for Mn, Cr and Co salts in catalytic degradation of dyes. *Appl. Clay Sci.* **2025**, *267*, 107721. [CrossRef]
26. El-Eswed, B.; Dawoud, J.N.; Albawarshi, Y.; Esaifan, M. The role of surface hydroperoxyl copper (I) in degradation of Congo red pollutant using copper oxide composites. *Int. J. Environ. Sci. Technol.* **2024**, *22*, 9245–9260. [CrossRef]
27. Bruziquesi, C.G.O.; Filho, J.B.G.; Mansur, H.S.; Chagas, P.; Mansur, A.A.P.; Oliveira, L.C.A.; Silva, A.C. New Niobate Based Catalyst for Organic Dye Oxidation: A Mechanistic Approach. *Water Air Soil Pollut.* **2024**, *235*, 679. [CrossRef]
28. Zhan, Y.Z.; Zhou, X.; Fu, B.; Chen, Y.L. Catalytic wet peroxide oxidation of azo dye (Direct Blue 15) using solvothermally synthesized copper hydroxide nitrate as catalyst. *J. Hazard. Mater.* **2011**, *187*, 348–354. [CrossRef]

29. Han, J.; Zeng, H.Y.; Xu, S.; Chen, C.R.; Liu, X.J. Catalytic properties of CuMgAlO catalyst and degradation mechanism in CWPO of methyl orange. *Appl. Catal. A Gen.* **2016**, *527*, 72–80. [CrossRef]
30. Xiao, X.Z.; Dai, T.T.; Guo, J.; Wu, J.H. Flowerlike Brochantite Nanoplate Superstructures for Catalytic Wet Peroxide Oxidation of Congo Red. *ACS Appl. Nano Mater.* **2019**, *2*, 4159–4168. [CrossRef]
31. Munoz, M.; Domínguez, P.; de Pedro, Z.M.; Casas, J.A.; Rodriguez, J.J. Naturally-occurring iron minerals as inexpensive catalysts for CWPO. *Appl. Catal. B Environ.* **2017**, *203*, 166–173. [CrossRef]
32. Ribeiro, R.S.; Frontistis, Z.; Mantzavinos, D.; Venieri, D.; Antonopoulou, M.; Konstantinou, I.; Silva, A.M.T.; Faria, J.L.; Gomes, H.T. Magnetic carbon xerogels for the catalytic wet peroxide oxidation of sulfamethoxazole in environmentally relevant water matrices. *Appl. Catal. B Environ.* **2016**, *199*, 170–186. [CrossRef]
33. Henrist, C.; Traina, K.; Hubert, C.; Toussaint, G.; Rulmont, A.; Cloots, R. Study of the Morphology of Copper Hydroxynitrate Nanoplatelets Obtained by Controlled Double Jet Precipitation and Urea Hydrolysis. *J. Cryst. Growth* **2003**, *254*, 176–187. [CrossRef]
34. Newman, S.P.; Jones, W. Comparative study of some layered hydroxide salts containing exchangeable interlayer anions. *J. Solid State Chem.* **1999**, *148*, 26–40. [CrossRef]
35. Pendashteh, A.; Rahmanifar, M.S.; Mousavi, M.F. Morphologically controlled preparation of CuO nanostructures under ultrasound irradiation and their evaluation as pseudocapacitor materials. *Ultrason. Sonochem.* **2014**, *21*, 643–652. [CrossRef] [PubMed]
36. Guillou, N.; Louër, M.; Louër, D. An X-Ray and Neutron Powder Diffraction Study of a New Polymorphic Phase of Copper Hydroxide Nitrate. *J. Solid State Chem.* **1994**, *109*, 307–314. [CrossRef]
37. Heinhold, R.; Williams, G.T.; Cooil, S.P.; Evans, D.A.; Allen, M.W. Influence of polarity and hydroxyl termination on the band bending at ZnO surfaces. *Phys. Rev. B* **2013**, *88*, 235315. [CrossRef]
38. Liu, B. One-Dimensional Copper Hydroxide Nitrate Nanorods and Nanobelts for Radiochemical Applications. *Nanoscale* **2012**, *4*, 7194–7198. [CrossRef]
39. Yu, Q.; Huang, H.W.; Chen, R.; Wang, P.; Yang, H.S.; Gao, M.X.; Peng, X.S.; Ye, Z.Z. Synthesis of CuO Nanowalnuts and Nanoribbons from Aqueous Solution and Their Catalytic and Electrochemical Properties. *Nanoscale* **2012**, *4*, 2613–2620. [CrossRef]
40. Huang, K.; Wang, J.J.; Wu, D.F.; Lin, S. Copper Hydroxyl Sulfate as a Heterogeneous Catalyst for the Catalytic Wet Peroxide Oxidation of Phenol. *RSC Adv.* **2015**, *5*, 8455–8462. [CrossRef]
41. Frost, R.L.; Leverett, P.; Williams, P.A.; Weier, M.L.; Erickson, K.L. Raman Spectroscopy of Gerhardtite at 298 and 77 K. *J. Raman Spectrosc.* **2004**, *35*, 991–996. [CrossRef]
42. Hu, Z.M.; Xiao, X.; Jin, H.Y.; Li, T.Q.; Chen, M.; Liang, Z.; Guo, Z.F.; Li, J.; Wan, J.; Huang, L.; et al. Rapid mass production of two-dimensional metal oxides and hydroxides via the molten salts method. *Nat. Commun.* **2017**, *8*, 15630. [CrossRef]
43. Biesinger, M.C.; Lau, L.W.M.; Gerson, A.R.; Smart, R.S.C. Resolving surface chemical states in XPS analysis of first row transition metals, oxides and hydroxides: Sc, Ti, V, Cu and Zn. *Appl. Surf. Sci.* **2010**, *257*, 887–898. [CrossRef]
44. Galeano, L.A.; Gil, A.; Vicente, M.A. Strategies for immobilization of manganese on expanded natural clays: Catalytic activity in the CWPO of methyl orange. *Appl. Catal. B Environ.* **2011**, *104*, 252–260. [CrossRef]
45. Kim, H.; Gang, B.; Jung, H.; Byeon, S.H. Cinnamate Intercalated-Layered Yttrium Hydroxide: A Potential Hybrid UV Filter. *J. Solid State Chem.* **2019**, *269*, 233–238. [CrossRef]
46. Yang, J.H.; Han, Y.S.; Park, M.P.T.; Hwang, S.J.; Choy, J.H. New Inorganic-Based Drug Delivery System of Indole-3-Acetic Acid-Layered Metal Hydroxide Nanohybrids with Controlled Release Rate. *Chem. Mater.* **2007**, *19*, 2679–2685. [CrossRef]
47. Solano, A.M.S.; Garcia-Segura, S.; Martínez-Huitle, C.A.; Brillas, E. Degradation of acidic aqueous solutions of the diazo dye Congo Red by photo-assisted electrochemical processes based on Fenton's reaction chemistry. *Appl. Catal. B Environ.* **2015**, *168–169*, 559–571. [CrossRef]
48. Granato, T.; Katovic, A.; Maduna Valkaj, K.; Tagarelli, A.; Giordano, G. Cu-silicalite-1 catalyst for the wet hydrogen peroxide oxidation of phenol. *J. Porous Mater.* **2009**, *16*, 227–232. [CrossRef]
49. Wang, L.S.; Kumeria, T.; Santos, A.; Forward, P.; Lambert, M.F.; Losic, D. Iron Oxide Nanowires from Bacteria Biofilm as An Efficient Visible-Light Magnetic Photocatalyst. *ACS Appl. Mater. Interfaces* **2016**, *8*, 20110–20119. [CrossRef]
50. Mi, L.W.; Wei, W.T.; Zheng, Z.; Gao, Y.; Liu, Y.; Chen, W.H.; Guan, X.X. Tunable properties induced by ion exchange in multilayer intertwined CuS microflowers with hierarchal structures. *Nanoscale* **2013**, *5*, 6589–6598. [CrossRef] [PubMed]
51. Yuan, G.G.; Zhang, G.Q.; Zhou, Y.F.; Yang, F.L. Synergetic adsorption and catalytic oxidation performance originating from leafy graphite nanosheet anchored iron(ii) phthalocyanine nanorods for efficient organic dye degradation. *RSC Adv.* **2015**, *5*, 26132–26140. [CrossRef]

Disclaimer/Publisher's Note: The statements, opinions and data contained in all publications are solely those of the individual author(s) and contributor(s) and not of MDPI and/or the editor(s). MDPI and/or the editor(s) disclaim responsibility for any injury to people or property resulting from any ideas, methods, instructions or products referred to in the content.